Control and Experiment of a TLC-MMC Hybrid DC–DC Converter for the Interconnection of MVDC and HVDC Grids

Shenghui Cui, *Student Member, IEEE*, Jingxin Hu, *Student Member, IEEE*, and Rik W. De Doncker, *Fellow, IEEE*

***Abstract*—An isolated bidirectional dc–dc converter, which combines parallel-connected two-level converters (TLCs) on the medium-voltage side and a modular multilevel converter (MMC) on the high-voltage side, namely a TLC-MMC converter, is a promising candidate for the interconnection of medium-voltage direct current (MVDC) and HVdc grids. Different from typical phase-shift controlled isolated bidirectional dc–dc converters, transformer currents of a TLC-MMC converter are regulated by the MMC in a closed-loop manner in order to achieve extremely low switching losses and low total device rating of power-semiconductor devices in TLCs. This paper addresses the dedicated operation technique and the voltage-balancing control of the TLC-MMC converter. The MMC in the TLC-MMC converter operates with six-step phase voltages and sinusoidal phase currents. Such an operation makes the MMC present remarkable differences to ac–dc applications. The direct-modulation technique, which is the most-used technique performed to MMCs in line-frequency ac–dc power conversion, has been concluded not applicable to the MMC in a TLC-MMC converter due to the significant sixth-order oscillation resulted in the dc-link voltage. Thus, the indirect-modulation technique is employed, and consequently a closed-loop voltage-balancing control is mandatory for the MMC. Possible measures for voltage balancing have been explored, and effective voltage-balancing control with a simplified implementation is proposed. Validity and effectiveness of the proposed control strategy have been verified by both simulations and experiment using a downscale prototype.**

***Index Terms*—DC grid, dc–dc converter, direct modulation indirect modulation, voltage-balancing control.**

I. Introduction

COMPARED to the existing ac grids, dc grids present several significant advantages such as high efficiency, high power density, flexibility, high controllability, no reactive power, free of bulky line-frequency transformer, etc. These advantages make the dc grid technology a promising solution to integrate large-scale renewable energies and energy storage systems, which call for more flexible and more controllable smart grids [1]–[3].

To build up such dc grids, an medium-voltage direct current (MVDC)-HVdc converter is one of the key components to interconnect MVDC distribution grids and HVdc transmission grids [4], [5]. In the past years, numerous topologies of high-power dc–dc converters including both nonisolated [6]–[9] and isolated [4], [10]–[14] types have been proposed and discussed. For the MVDC-HVdc power conversion, where the voltage step-up ratio is high ($V_{\mathrm{dc,HV}}/V_{\mathrm{dc,MV}} > 5$), galvanic isolation is preferred not only for safety but also to reduce total device ratings and losses of power-semiconductor devices [13].

The two-level converter(TLC) modular multilevel converter (MMC) converter proposed in [14], which combines multiple three-phase TLCs in parallel on the MV side and a three-phase MMC on the HV side as shown in Fig. 1, is a promising candidate for this application. The TLC-MMC converter presents low-power semiconductor total device rating and low semiconductor losses over a wide power range at variable input and output voltages.

This paper aims to providing an insight into the control strategy of the TLC-MMC converter and verifying it with experimental results. In a TLC-MMC converter, the TLCs operate in the six-step mode in an open-loop manner, and the MMC controls transformer currents in a closed-loop manner in order to achieve low switching losses and low total device rating of power-semiconductor devices in the TLCs.

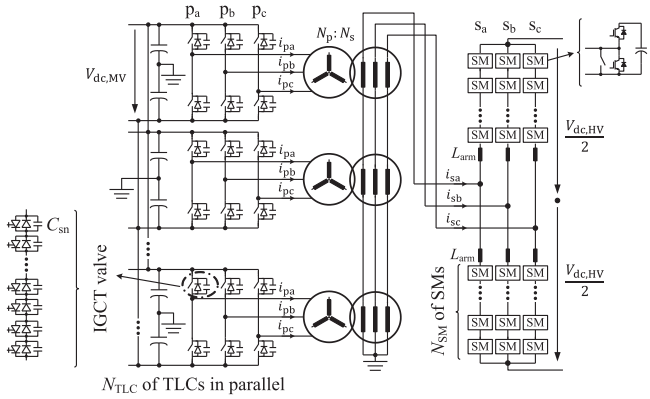

Fig. 1. Configuration of a TLC-MMC hybrid dc–dc converter.

Manuscript received November 22, 2018; revised March 1, 2019 and May 9, 2019; accepted July 3, 2019. Date of publication July 11, 2019; date of current version December 13, 2019. This work was supported by the German Federal Ministry of Education and Research (BMBF) within the Kopernikus Project ENSURE "NeueEnergieNetzStruktURen für die Energiewende" under Project 03SFK1C0. Recommended for publication by Associate Editor M. Saeedifard. *(Corresponding author: Shenghui Cui.)*

The authors are with the Institute for Power Generation and Storage Systems E.ON Energy Research Center, RWTH Aachen University, Aachen 52062, Germany (e-mail: cuish0704@gmail.com; Jingxin.Hu@isea.rwth-aachen.de; dedoncker@ieee.org).

Color versions of one or more of the figures in this paper are available online at http://ieeexplore.ieee.org.

Digital Object Identifier 10.1109/TPEL.2019.2928258

The stable operation of the TLC-MMC converter is highly dependent on the MMC operation. Operation techniques of MMCs are generally classified into the direct-modulation-based operation and indirect-modulation-based operation [15], [16]. In the direct-modulation technique, a modulation index is acquired by nominal submodule (SM)-capacitor voltages. The main advantage of such a technique is the self-balancing capability of arm SM-capacitor voltages. However, it presents a major drawback of the presence of a considerable second-order circulating current due to fluctuations of SM-capacitor voltages. The second-order circulating current can be suppressed by employing an additional circulating current suppression controller [17]. In the indirect-modulation technique, a modulation index is acquired by measured SM capacitor voltages. It inherently presents no second-order circulating current, whereas voltage balancing of arm SM-capacitor voltages is marginally stable, and a closed-loop control should be applied to maintain voltage balance [16]. The direct-modulation technique is mostly used in HVdc applications [17]–[23], where an MMC converts power from line-frequency ac to dc, due to its simple structure of controllers.

In a TLC-MMC converter, the voltage on the ac side of the MMC is in a form of six steps. If the direct-modulation technique is employed, it can realize desired transformer-current control and voltage balancing of SMs as well as in ac–dc power conversions. However, it has been proven in this study that a serious voltage oscillation issue can be induced in the dc link on the HV side. This can result in a significant oscillation current propagating into the connected HVdc cable. It is first revealed in this paper that, an MMC presents a unique feature of sixth-order oscillation in the dc-link voltage when the ac-side voltage is of six steps. Such an oscillation inherently results from the fifth- and seventh-order harmonics in the ac-side six-step voltage.

In order to avoid the aforementioned oscillation issue, the indirect-modulation-based operation is performed to the MMC. This brings a new challenge to voltage-balancing control since the existing knowledge is limited to ac–dc power conversion where the ac-side voltage is sinusoidal. Different possible measures for voltage balancing are explored, and an effective voltage-balancing control with a simplified implementation is proposed in this paper. Thus, the voltage-balancing issue can be successfully addressed, and the voltage oscillation in the dc link of the MMC can be fully avoided. In addition, experimental verifications of a TLC-MMC converter are first presented by a 60 V/250 V, 1-kW downscale laboratory prototype.

II. Operation Principle and Transformer-Current Control

A TLC-MMC converter includes a number N_{TLC} of TLCs in parallel on the MV side. They are connected via the same number of open-end winding transformers to an MMC on the HV side as shown in Fig. 1. The ac outputs of the TLCs are connected to the primary sides of the transformers, and the secondary sides of the transformers are connected in series in order to boost the voltage. The number N_{TLC} is determined by the current rating on the MV side.

Each TLC on the MV side is based on integrated gate-commutated thyristors (IGCTs) for higher current rating and lower conduction loss [14]. A certain number of IGCTs are connected in series to form an IGCT valve as shown in Fig. 1, which can withstand the MV-side dc-link voltage. Due to the series connection of IGCTs, the snubber capacitors in parallel are mandatory for dynamic voltage balancing [24]. Due to the presence of the snubber capacitors, IGCTs should be always turned ON at zero voltage after the snubber capacitors in parallel are fully discharged in order to protect themselves against an uncontrolled rate of di/dt [25], [26].

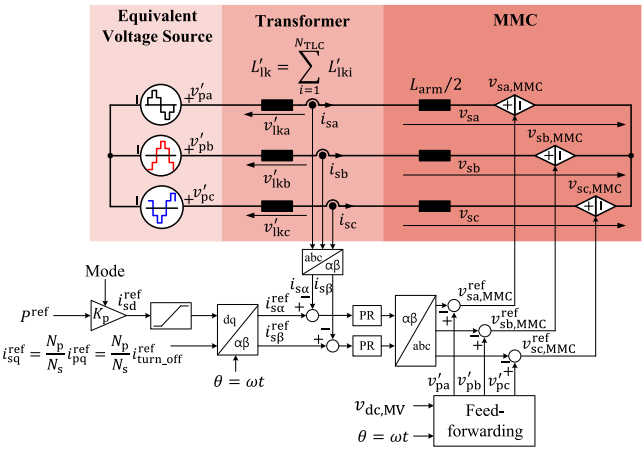

Fig. 2. Transformer-current model and the block diagram of the transformer-current controller.

The TLCs on the MV side operate synchronously in the six-step mode in an open-loop manner, and they are equivalent to a single equivalent TLC referred to the MMC side as shown in Fig. 2. The MMC on the HV side controls the transformer's secondary-side current in a closed-loop manner in a sinusoidal form in order to suppress the transformer stray loss caused by the leakage fluxes of harmonic currents [27]. Due to the series connection of the transformers' secondary sides, the primary-side currents of the transformers are driven by the MMC's ac-side current uniformly. Thus, a circulating current between TLCs is inherently prevented.

In the transformer-current controller, the instantaneous phase voltages generated by the TLCs are calculated online by the feed-forwarding block in Fig. 2. The power transfer of the TLC-MMC converter is linear with respect to the active current i_{sd} generated by the MMC, and its reference $i_{\mathrm{sd}}^{\mathrm{ref}}$ comes from the power reference P^{ref}. Note that the turn-OFF current $i_{\mathrm{turn\_off}}$ of a TLC operating in the six-step mode is identical to the reactive current. Thus, the MMC also draws a certain amount of inductive reactive current to discharge the snubber capacitors in order to realize zero-voltage switching (ZVS) in the TLCs. The reactive-current reference $i_{\mathrm{sq}}^{\mathrm{ref}}$ is set constant to a certain value, which is high enough to fully discharge the snubber capacitors within the dead time for ZVS of IGCT valves in the TLCs but still much smaller than the rated active current.

With such an operation method, the switch valves in the TLCs are always turned OFF at a very low current and are turned ON at zero voltage, and the TLCs operate virtually in a zero-switching-loss manner. Consequently, conduction optimized IGCTs with minimized on-state voltages can be employed to further decrease the overall losses in the TLCs. In typical phase-shift controlled

isolated dc–dc converters used in high-power applications, e.g., dual-active bridges (DAB), auxiliary circuits should be installed and activated in partial-load conditions in order to assist discharging of snubber capacitors within the dead time [25], [26]. Due to the losses caused by the activation of the auxiliary circuits, the efficiency of the converter is significantly degraded in partial-load conditions [34]. However, the functionality of these auxiliary circuits is covered by the MMC via drawing a small reactive current. Thus, the TLC-MMC converter can achieve low semiconductor losses not only in the full-load condition but also in light-load conditions. In accordance with calculations, the light-load efficiency at 10% of the rated power is almost identical to that in the full-load condition [14]. More details on the loss calculations and the characteristics of the TLC-MMC converter are found in [14].

III. Operation Technique of MMC

To the best knowledge of the authors, operation characteristic of an MMC operating with a six-step ac-side voltage in conjunction with the direct-modulation technique has never been investigated.

In the direct modulation, the modulation indexes of both upper and lower arms $n_{\rm ux}^{\rm ref}$ and $n_{\rm lx}^{\rm ref}$ in an arbitrary "*x*" phase are obtained directly via the nominal SM-capacitor voltage $V_{\rm SM}$ as (1), where $v_{\rm ux}^{\rm ref}$ and $v_{\rm lx}^{\rm ref}$ are the arm terminal voltage references of upper and lower arms, respectively. The variable $v_{\rm sx,MMC}^{\rm ref}$ is the ac-side output voltage reference of the MMC shown in Fig. 2

$$\begin{cases} n_{\rm ux}^{\rm ref} = \frac{v_{\rm ux}^{\rm ref}}{N_{\rm SM}V_{\rm SM}} = \frac{0.5V_{\rm dc,HV}-v_{\rm sx,MMC}^{\rm ref}}{N_{\rm SM}V_{\rm SM}} \\ n_{\rm lx}^{\rm ref} = \frac{v_{\rm lx}^{\rm ref}}{N_{\rm SM}V_{\rm SM}} = \frac{0.5V_{\rm dc,HV}+v_{\rm sx,MMC}^{\rm ref}}{N_{\rm SM}V_{\rm SM}}. \end{cases} \tag{1}$$

If the sums of the instantaneous SM-capacitor voltages, namely the arm capacitor voltages of both upper and lower arms are $v_{\rm SM,ux}^{\Sigma}$ and $v_{\rm SM,lx}^{\Sigma}$, respectively, then the terminal voltages of both arms are (2). Since modulation indexes are not obtained via the measured SM capacitor voltages, arm terminal voltages are synthesized with errors with respect to their references

$$\begin{cases} v_{\rm ux} = n_{\rm ux}^{\rm ref} v_{\rm SM,ux}^{\Sigma} = \left(0.5V_{\rm dc,HV} - v_{\rm sx,MMC}^{\rm ref}\right) \frac{v_{\rm SM,ux}^{\Sigma}}{N_{\rm SM}V_{\rm SM}} \neq v_{\rm ux}^{\rm ref} \\ v_{\rm lx} = n_{\rm lx}^{\rm ref} v_{\rm SM,lx}^{\Sigma} = \left(0.5V_{\rm dc,HV} + v_{\rm sx,MMC}^{\rm ref}\right) \frac{v_{\rm SM,lx}^{\Sigma}}{N_{\rm SM}V_{\rm SM}} \neq v_{\rm lx}^{\rm ref}. \end{cases} \tag{2}$$

Since an MMC inherently includes three individual phases, single-phase power fluctuation results in oscillations in the SM-capacitor voltages if the ac-side current is not zero. It has been analyzed mathematically that a fundamental-frequency and a second-order fluctuations exist in the SM-capacitor voltages [28]. The second-order fluctuations in the upper and lower arms are with the same magnitudes and polarities. However, the fundamental-frequency fluctuations are with the same magnitudes but opposite polarities. The instantaneous arm capacitor voltages of both arms can be represented as (3), where the symbol $\bar{v}$ presents the dc mean value and the symbol $\tilde{v}$ presents the fluctuating component. In the steady state, the dc mean voltages of the arm capacitors of both arms $\bar{v}_{\rm SM,ux}^{\Sigma}$ and $\bar{v}_{\rm SM,lx}^{\Sigma}$ are $N_{\rm SM}V_{\rm SM}$. It is noted that the voltage fluctuations are linear with respect to the magnitude of the ac-side sinusoidal current, and they diminish in the no-load situation

$$\begin{cases} v_{\rm SM,ux}^{\Sigma} = \bar{v}_{\rm SM,ux}^{\Sigma} + \tilde{v}_{\rm SM,x,\omega}^{\Sigma} + \tilde{v}_{\rm SM,x,2\omega}^{\Sigma} \\ v_{\rm SM,lx}^{\Sigma} = \bar{v}_{\rm SM,lx}^{\Sigma} - \tilde{v}_{\rm SM,x,\omega}^{\Sigma} + \tilde{v}_{\rm SM,x,2\omega}^{\Sigma}. \end{cases} \tag{3}$$

The spectrums of the arm terminal voltage and the leg terminal voltage are presented in Fig. 3. From (2) the arm terminal voltage is the convolution of the modulation index and the arm capacitor voltage in the frequency domain. In the spectrum of the arm capacitor voltage, all components are identical in magnitude in both arms, whereas the fundamental-frequency components present opposite polarities. In the spectrum of the modulation index, all the ac components are with opposite polarities as indicated by (1). A significant difference compared to the case of grid-connected applications is that the ac components include not only the fundamental-frequency component but also the fifth- and seventh-order harmonics, which are depicted in blue and red, respectively. These two harmonic components in the modulation index result in various components in the arm terminal voltages including third- to ninth-order harmonics, as shown in the gray area of Fig. 3. Note that the leg terminal voltage at each phase is the sum of the arm terminal voltages of the upper and lower arms. Thus, the odd-order harmonics vanish in the leg terminal voltage due to the opposite polarities in the arm terminal voltages, and the even-order harmonics remain in the leg terminal voltage. Note that the fourth-, sixth-, and eighth-order harmonics do not exist in the leg terminal voltage in grid-connected applications [28].

Fig. 4 shows the equivalent circuit to describe the dc-side current of the MMC. The ripple voltages across a leg terminal include second-, fourth-, and eighth-order harmonics, which are differential mode, and a sixth-order harmonic, which is common mode. In accordance with the Thévenin's theorem, the differential mode ripple voltages do not present to the dc side. However, they result in a significant circulating current at the corresponding frequencies [17], [28] if no countermeasure is taken. The common mode ripple voltage generates a harmonic current that flows into the transmission line. The dc link of the MMC is supposed to connect to an HVdc transmission grid via an HVdc cable. The magnitude of the resulted sixth-order ripple current is dependent on the sum of the impedance of the arm inductor $L_{\rm arm}$ and the impedance at the sending end of the HVdc cable $Z_{\rm send}$.

The simulation results of the HV-side dc-link voltage and current of the TLC-MMC converter are shown in Fig. 5 when the cable length is 31.6 km, which corresponds to one fourth of the wavelength $\lambda_{\rm 6th}$ at the sixth-order harmonic frequency. The power flows from the HV side to the MV side, and it increases from 0 to 1 p.u. at $t = 0.5$ s. The simulation parameters are identical to the simulation study in Section V. The impedance at the receiving end (HVdc grid) of the cable is approximated to be zero [29]. Thus, the impedance at the sending end of the HVdc cable presents the maximum when the cable length is $\lambda_{\rm 6th}/4$ [29]. Consequently, the sixth-order ripple current is suppressed well even though a significant voltage oscillation exists.

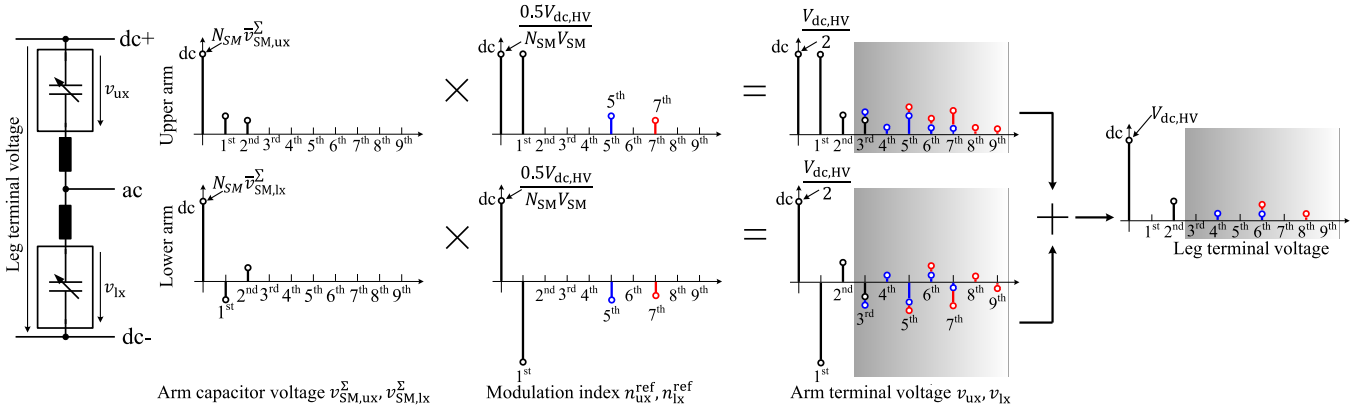

Fig. 3. Analysis of arm terminal voltages and the corresponding leg terminal voltage of "x" phase in the frequency domain.

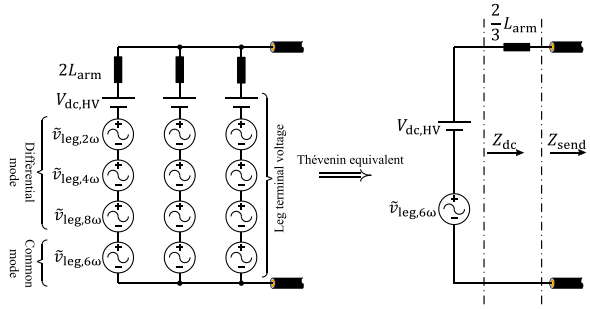

Fig. 4. Equivalent circuit for the dc-side harmonic current of the MMC operating in the six-step mode.

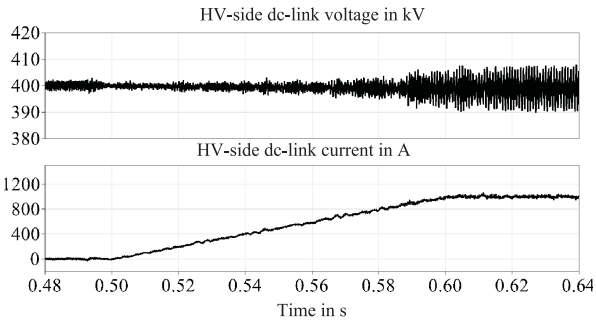

Fig. 5. Simulation results of the direct-modulation based operation when the HVDC cable length is 31.6 km.

However, the cable impedance is very sensitive to the cable length. A dramatic difference occurs when the cable length increases to 48 km as shown in Fig. 6. A significant sixth-order harmonic current is induced with respect to the increased power, and the magnitude in the steady state when the power is 1 p.u. is as high as 230 A. Such a ripple current in the dc link not only increases the transmission loss in the cable resulting in hot spots but also might lead to malfunction of the protection system in the dc grid [30].

It is well known that the isolated dc–dc converters operating in six-step mode, e.g., three-phase DABs [34] and three-phase series-resonant converters (SRCs) [35] also feature sixth-order ripple currents in the dc-link. However, the sixth-order ripple currents in these types of dc–dc converters originate from a different reason and present different characteristics as shown

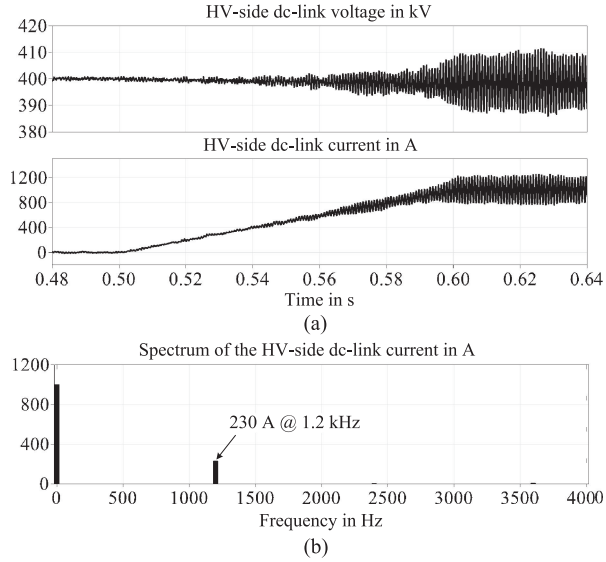

Fig. 6. Simulation results of the direct-modulation based operation when the HVDC cable length is 48 km: HV-side voltage and current in (a) the time domain and (b) the frequency domain.

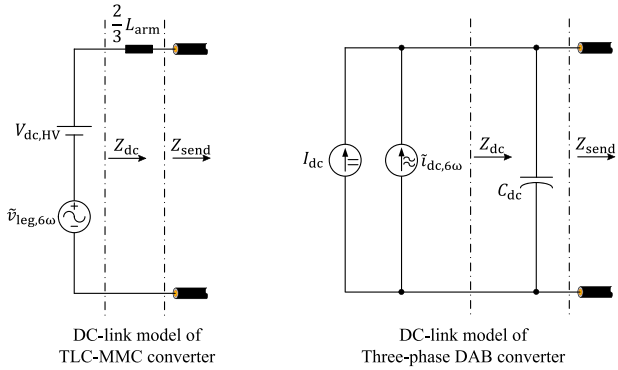

Fig. 7. Comparison of dc-link models of the TLC-MMC converter and the three-phase DAB.

in Fig. 7. In three-phase DABs and SRCs, the dc-link current results from a superposition of chopped transformer currents in three phases, which are phase shifted by 120°. The superposition of the chopped transformer currents features a dc component I_{dc} and a sixth-order ripple $\tilde{i}_{\mathrm{dc},6\omega}$ [34], and the magnitudes of

both dc component and sixth-order ripple are only determined by the transformer currents. Thus, from the connected cable side, the dc link of a three-phase DAB or SRC is equal to two current sources in parallel behind the dc-link capacitor. Thus, the sixth-order ripple current, which flows into the cable, is limited up to $\tilde{i}_{\mathrm{dc},6\omega}$ in Fig. 7 in the worst case. The magnitude of $\tilde{i}_{\mathrm{dc},6\omega}$ can be calculated analytically, and the ripple current flows into the cable is usually limited by a proper design of the dc-link capacitance C_{dc}. However, in the TLC-MMC converter the sixth-order ripple current that flows into the cable is driven by voltage ripple $\tilde{v}_{\mathrm{leg},6\omega}$, which originates from the SM capacitor voltage ripples, and its magnitude is determined by the arm inductor and the cable impedance. In the worst case, when the cable impedance is capacitive and tends to counter with $\frac{2}{3}L_{\mathrm{arm}}$, a significant ripple current could flow into the cable.

The second-, fourth, and eighth-order circulating currents resulted from the differential mode ripple voltages in the leg terminal voltage in Fig. 4 could be suppressed by employing circulating current suppression controllers. Note that the fundamental frequency of the transformer is in a range of hundreds Hz (typically 200–500 Hz) [11], controlling the harmonic currents in a closed loop is challenging regarding the sampling ratio of the digital controller at the corresponding harmonic frequencies.

IV. Voltage-Balancing Control

The sixth-order oscillation in the dc-link voltage discussed in Section III is attributed to two aspects. The first reason is that fifth- and seventh-order harmonics are included in the references of the arm terminal voltages due to the six-step voltage. The second reason is that the modulation index is obtained via the nominal SM capacitor voltage. Thus, the ripples in the SM capacitor voltages in conjunction with the harmonics included in the reference of the arm terminal voltage result in the oscillation in the dc-link voltage as expressed in (2).

Since the harmonics intrinsically exist in the reference of the arm terminal voltage, the unique way to eliminate the sixth-order voltage oscillation in the dc link is to avoid the synthesis error of the arm terminal voltage introduced by the direct modulation. The indirect-modulation-based operation is an effective way to address this problem, where the modulation index is obtained via the measured SM capacitor voltages as (4). Thereby, the arm terminal voltages can be synthesized without errors with respect to the references as (5), and the sixth-order oscillation voltage in the dc link is eliminated since no sixth-order component is included in the arm terminal voltage any more

$$\begin{cases} n_{\mathrm{ux}}^{\mathrm{ref}} = \dfrac{v_{\mathrm{ux}}^{\mathrm{ref}}}{v_{\mathrm{SM,ux}}^{\Sigma}} = \dfrac{0.5V_{\mathrm{dc,HV}} - v_{\mathrm{sx,MMC}}^{\mathrm{ref}}}{v_{\mathrm{SM,ux}}^{\Sigma}} \\ n_{\mathrm{lx}}^{\mathrm{ref}} = \dfrac{v_{\mathrm{lx}}^{\mathrm{ref}}}{v_{\mathrm{SM,ux}}^{\Sigma}} = \dfrac{0.5V_{\mathrm{dc,HV}} + v_{\mathrm{sx,MMC}}^{\mathrm{ref}}}{v_{\mathrm{SM,ux}}^{\Sigma}} \end{cases} \tag{4}$$

$$\begin{cases} v_{\mathrm{ux}} = n_{\mathrm{ux}}^{\mathrm{ref}} v_{\mathrm{SM,ux}}^{\Sigma} = \left(0.5V_{\mathrm{dc,HV}} - v_{\mathrm{sx,MMC}}^{\mathrm{ref}}\right) \dfrac{v_{\mathrm{SM,ux}}^{\Sigma}}{v_{\mathrm{SM,ux}}^{\Sigma}} = v_{\mathrm{ux}}^{\mathrm{ref}} \\ v_{\mathrm{lx}} = n_{\mathrm{lx}}^{\mathrm{ref}} v_{\mathrm{SM,lx}}^{\Sigma} = \left(0.5V_{\mathrm{dc,HV}} + v_{\mathrm{sx,MMC}}^{\mathrm{ref}}\right) \dfrac{v_{\mathrm{SM,lx}}^{\Sigma}}{v_{\mathrm{SM,ux}}^{\Sigma}} = v_{\mathrm{lx}}^{\mathrm{ref}}. \end{cases} \tag{5}$$

However, in order to apply the indirect-modulation-based technique to avoid the sixth-order oscillation in the dc link, the voltage-balancing issue must be addressed. It is well known that the voltage balancing among six arms of the MMC is intrinsically marginally stable when the indirect-modulation-based operation is performed. Thus, a closed-loop voltage-balancing control is mandatory to sustain the voltage balance. A common control strategy performed to an MMC in sinusoidal ac–dc conversions is injecting circulating currents inside the MMC [31], [32] temporarily in case of a voltage imbalance in order to circulate power among six arms for the voltage balancing. The injected circulating currents vanish automatically as long as the arm capacitor voltages are balanced.

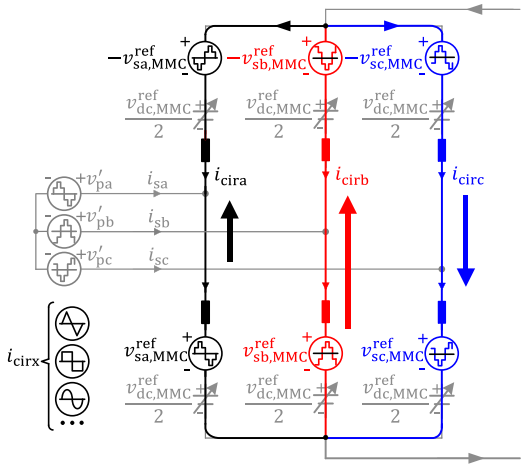

Fig. 8. Principle of the arm voltage balancing control inside each phase.

The voltage balancing among three-phase legs is realized by injecting a dc circulating current since three legs share the same dc-link voltage. The voltage balancing between upper and lower arms inside each leg is realized via injecting a sinusoidal ac circulating current since the sinusoidal voltages included in the upper and lower arm terminal voltages are identical in magnitude but opposite in polarity as (1). The dynamics of the arm capacitor energy imbalance of an arbitrary "x" phase E_{x}^{Δ} are characterized in (6)

$$\frac{dE_{\Delta\mathrm{x}}}{dt} = \frac{\mathrm{d}\left(E_{\mathrm{ux}} - E_{\mathrm{lx}}\right)}{\mathrm{d}t} = P_{\Delta\mathrm{x}} = -2v_{\mathrm{sx,MMC}}^{\mathrm{ref}} i_{\mathrm{cirx}}. \tag{6}$$

However, the ac-side voltage reference of the MMC $v_{\mathrm{sx,MMC}}^{\mathrm{ref}}$ in the TLC-MMC converter includes a six-step voltage and a sinusoidal voltage across the transformer leakage inductor, and the six-step voltage is dominant in magnitude. This introduces a problem of determining the form of the circulating current to inject and the implementation of the circulating-current reference generation and regulation.

Regarding the form of the injected circulating current, any ac form of a circulating current, which can contribute a dc mean power in conjunction with $v_{\mathrm{sx,MMC}}^{\mathrm{ref}}$ in (6), e.g., a triangular or a rectangular waveform, can be utilized for arm capacitor voltage balancing as depicted in Fig. 8. In closed-loop current control point of view, a sinusoidal current form is optimal since it does not include any other harmonic component. In addition, an optimal form is preferred to be with a frequency as low as

possible when the digital control delay is taken into account so that the sampling ratio can be maximized.

As discussed in Section III, $v^{\mathrm{ref}}_{\mathrm{sx,MMC}}$ includes not only the fundamental-frequency voltage but also fifth-order and seventh-order harmonic voltages, since it is dominated by the six-step voltage. It means that, either a fundamental-frequency or a fifth-order (or seventh-order) sinusoidal circulating current can transfer an active power (namely with a dc mean value of $P_{\Delta\mathrm{x}}$) between arms in accordance with (6). The fundamental-frequency circulating current is regarded as the optimal one for the following two reasons. First, the fundamental-frequency voltage in $v^{\mathrm{ref}}_{\mathrm{sx,MMC}}$ is the largest in magnitude. In accordance with the spectrum analysis, the magnitudes of the fifth-order and the seventh-order harmonic voltages are one fifths and one sevenths of that of the fundamental-frequency voltage. Thus, the fundamental-frequency circulating current injection requires the minimum current in magnitude to transfer the same amount of power between upper and lower arms for arm capacitor voltage balancing. Second, the lower frequency of the fundamental-frequency current can significantly simplify the efforts to the closed-loop digital current control. If the transformer operates at a frequency of 200 Hz, then the fifth-order harmonic current is with a frequency of as high as 1 kHz, which calls for a high sampling frequency of the digital controller resulting in remarkable efforts in engineering implementation.

Another issue of the voltage balancing comes in the generation of the circulating-current reference. The fundamental-frequency component in $v^{\mathrm{ref}}_{\mathrm{sx,MMC}}$ should be extracted online for the voltage orientation and generating the reference of the circulating current. The online Fourier transformation not only increases the computational burden but also leads to a delay. In this paper, a simplified voltage extraction method is proposed.

The fundamental-frequency component in $v^{\mathrm{ref}}_{\mathrm{sx,MMC}}$, namely ${}^{1}v^{\mathrm{ref}}_{\mathrm{sx,MMC}}$ includes two parts, which are the part ${}^{1}v'_{\mathrm{px}}$ included in the six-step voltage v'_{px} of the equivalent TLC in Fig. 2 and the part across the transformer leakage inductor $j\omega L'_{\mathrm{lk}} i_{\mathrm{sx}}$. Note that the fundamental-frequency component of the six-step voltage is always in phase with the six-step voltage, and its magnitude is only determined by the instantaneous dc-link voltage. Thus, the first part ${}^{1}v'_{\mathrm{px}}$ can be calculated by the phase angle θ and the dc-link voltage $v_{\mathrm{dc,MV}}$. The second part $j\omega L'_{\mathrm{lk}} i_{\mathrm{sx}}$ can be calculated in the stationary $\alpha\beta$ reference frame by the measured transformer current i_{sx}.

The block diagram of the proposed arm voltage-balancing controller for the TLC-MMC converter is shown in Fig. 9. The fundamental-frequency component of $v^{\mathrm{ref}}_{\mathrm{sx,MMC}}$ is extracted via the aforementioned technique, and the circulating-current reference $i^{\mathrm{ref}}_{\mathrm{cirx,ac}}$ is generated by the reference of the circulating power $P^{\mathrm{ref}}_{\Delta\mathrm{x}}$ and the extracted voltage component ${}^{1}v^{\mathrm{ref}}_{\mathrm{sx,MMC}}$ in accordance with (6). By the proposed method, the arm capacitor voltage balancing can be realized via the minimum injected current and the minimum effort for the implementation.

Besides the voltage balancing, the total energy stored in the SMs of the MMC should be regulated to its nominal value as well in order to sustain the capacitor voltages of each arm at the nominal voltage. The total energy is controlled by regulating

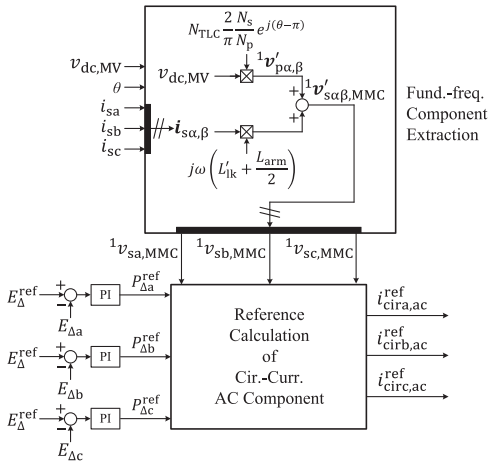

Fig. 9. Block diagram of the proposed arm voltage balancing controller for the TLC-MMC converter.

the HV-side dc-link power, namely the dc-link current. The dc-link current is controlled in a closed-loop manner, since the dc-side of the MMC acts as a controlled voltage source behind an equivalent inductor to the connected cable, when the indirect-modulation technique is performed [31], [32].

To summarize, the indirect-modulation-based operation gets fully applicable to the MMCs operating with six-step phase voltages when the proposed voltage-balancing control is employed. It should be noted that the injected dc and fundamental-frequency circulating currents occur only in case of the voltage imbalance, and they become automatically nullified when arm capacitor voltages are balanced. In addition, different from the case of the direct-modulation-based operation there is no harmonic circulating current or sixth-order harmonic dc-link current in the steady state. Thus, operation of the MMC with minimal losses is assured with the proposed indirect-modulation-based operation.

V. Simulation Results

To verify the proposed control strategy, a $\pm$25 kV/$\pm$200 kV, 400-MW TLC-MMC converter is simulated using PLECS software. The detailed parameters of the simulated converter are presented in Table I. The sampling frequency of the digital controller is 12 kHz. Over the whole operation range, the MMC injects a reactive current to the TLCs in order to ensure ZVS of IGCTs. The magnitude of the reactive current reference on the primary side is set to 100 A, whereas the rated active current on the primary side is 4.2 kA, which is much higher than the reactive current. The HV-side dc link is connected to a $\pm$200 kV HVdc grid via a cable at a length of 48 km, which is identical to the case in Fig. 6.

Fig. 10 presents the simulation results of a power reference reversal from 1 to –1 p.u., when the proposed operation scheme based on the indirect modulation is performed to the MMC. Different from the results of the direct modulation controlled MMC presented in Fig. 6, the sixth-order oscillation voltage and current are fully eliminated in the dc link in the full-load situations,

TABLE I
PARAMETERS OF THE SIMULATED TLC-MMC CONVERTER

MV-side TLCs (50 kV_{dc}, 200 MW)	
Converter quantity (N_{TLC})	2
Switch	4.5 kV device ×20 per valve
Snubber capacitor (C_{sn})	1 μF
Transformers (200 Hz)	
Transformer quantity	2
Turns ratio (N_p: N_s)	9:22
Leakage inductance (L'_{lk})	10 mH (27.6 % at 200 Hz)
HV-side MMC (400 kV_{dc}, 400 MW)	
Number of SMs (N_{SM})	216 per arm (8 % redundancy)
Rated SM voltage ($V_{SM,cap}$)	2.2 kV
SM capacitor	1.13 mF
Arm inductor (L_{arm})	15 mH
HVDC Cable	
Resistance	0.0178 Ω/km
Capacitance	0.275 μF/km
Inductance	0.158 mH/km

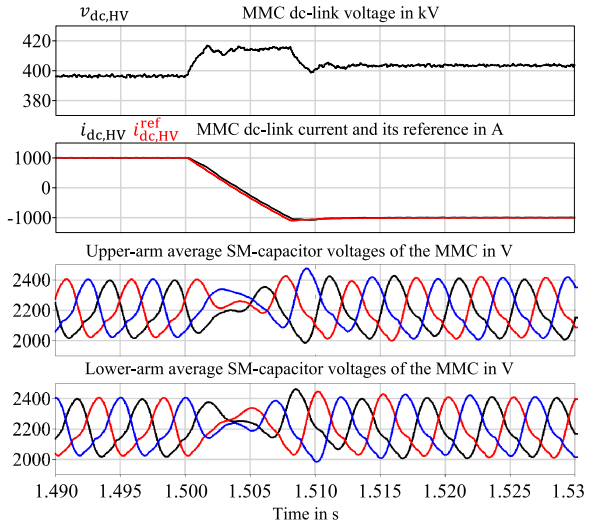

Fig. 10. Simulation results when the power reverses from 1 pu to −1 pu.

and the dc-link current tracks its reference with an acceptable dynamic performance. With the proposed voltage-balancing control, the average SM-capacitor voltages of both upper and lower arms in all three phases are regulated successfully at the rated voltage 2.2 kV in both the dynamic process and steady states.

Simulation results are shown in Fig. 11 in case an HVdc-grid voltage sag occurs from 400 to 380 kV abruptly when the power flow is –1 p.u. The dc-link voltage of the MMC decreases accordingly due to the closed-loop control of the dc-link current, and the magnitude of the dc-link current increases in order to sustain the presag power. Stepwise oscillating disturbances are observed in both the dc-link voltage and current of the MMC. These disturbances are induced by the traveling waves along the HVdc cable, which are induced by the abrupt voltage sag from the HVdc grid, and they are damped by the cable resistances afterward. In such a dynamic process, the average SM-capacitor voltages of both upper and lower arms in all three phases are well

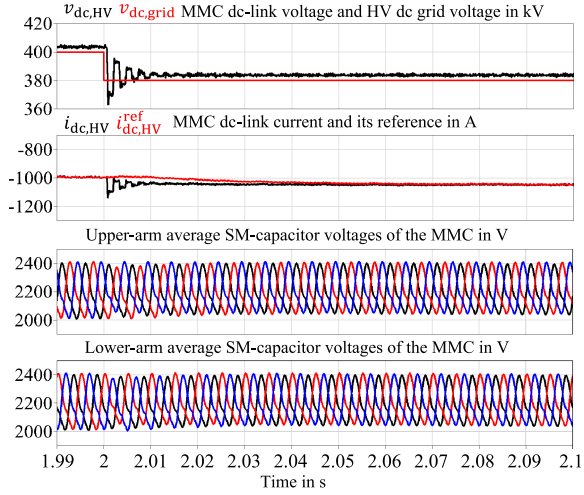

Fig. 11. Simulation results in case an abrupt HVDC grid voltage sag occurs when the power flow is −1 pu.

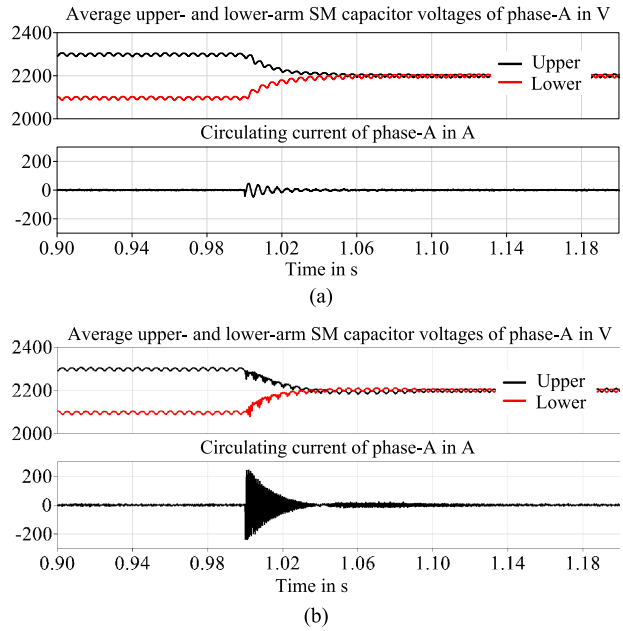

Fig. 12. Simulation results of the arm capacitor voltage balancing control, when the (a) fundamental-frequency and the (b) 5th-order circulating currents are injected for the voltage balancing.

balanced and are regulated at the rated voltage by the proposed voltage-balancing control.

Simulation results of the arm capacitor voltage balancing are presented in Fig. 12(a) and (b), where the balancing controls based on the injections of the fundamental-frequency and the fifth-order harmonic circulating currents are compared. The PI parameters of the balancing controller shown in Fig. 9 are set identical in order to observe the injected circulating current with identical balancing dynamics. The balancing controller is activated at $t = 1.0$ s. As shown in Fig. 12, the upper and lower arm capacitor voltages converge to the balanced state with an identical dynamic process in both cases.

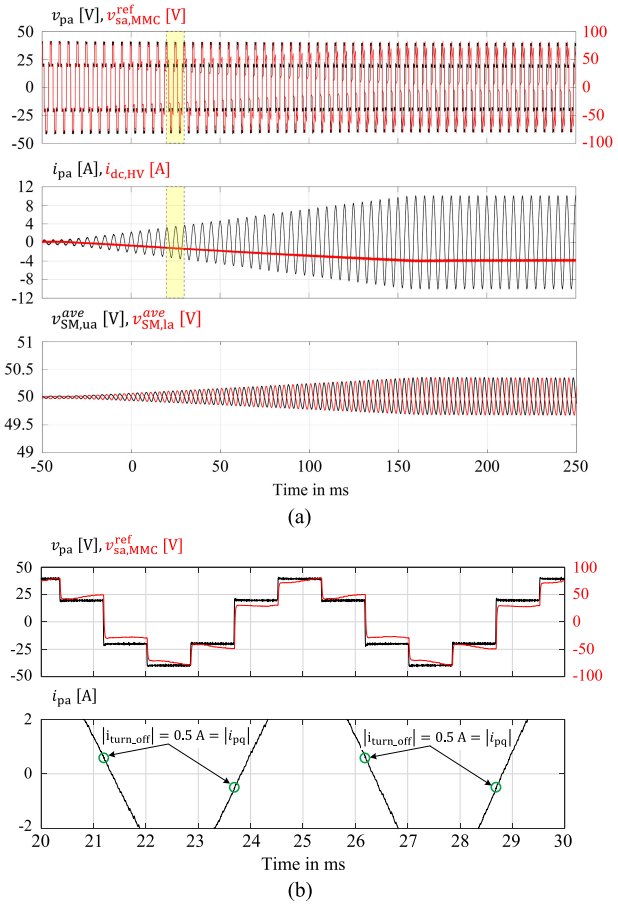

Fig. 13. Experimental results when the power varies from 0 pu to −1 pu: (a) results in the complete process, (b) results in the zoomed time scale.

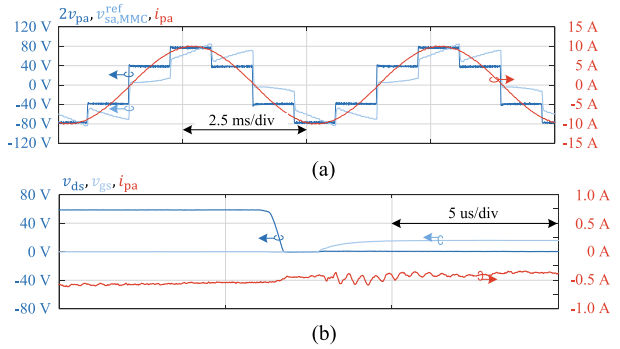

Fig. 14. Steady-state experimental results when the power is −1 pu, (a) TLC phase voltage and current, and the ac-side voltage reference of the MMC, (b) the blocking voltage and the gate voltage of a switch, and the phase current in the corresponding TLC.

However, the magnitude of the fifth-order harmonic current is five times of that of the fundamental-frequency current, which coincides with the analysis in Section IV. The higher magnitude of the fifth-order harmonic current introduces higher conduction loss and higher current stress to the semiconductor devices. Thus, the fundamental-frequency circulating current presents an optimal performance at a minimal cost of the current magnitude.

VI. Experimental Verifications

A 60 V/250 V, 1-kW downscale prototype is built up and tested to verify the proposed control method. The prototype includes two TLCs, two multiwinding open-end transformers (turns ratio 1:1) and an MMC. The MMC includes 5 SMs per arm, with a nominal SM voltage of 50 V and an SM capacitance of 5.4 mF. The arm inductance is 4 mH, and the sampling frequency of the digital controller is 12 kHz. The magnitude of the reactive current reference on the primary is constantly set to 0.5 A, whereas the rated active current on the primary side is 10 A, which is much higher than the reactive current.

Experimental results shown in Fig. 13 present the case of a load power ramp from 0 to –1 p.u., when the proposed indirect-modulation-based control is performed to the MMC. The transformer current and the HV-side dc-link current are well controlled in the dynamic process, and the sixth-order oscillation voltage and current are fully eliminated as shown in Fig. 13(a). With the proposed voltage-balancing control method, the average SM capacitor voltages of both upper and lower arms of phase "a" $v^{\text{ave}}_{\text{SM,ua}}$ and $v^{\text{ave}}_{\text{SM,la}}$ are well balanced, and their dc mean voltages are controlled at the rated voltage of 50 V. The turn-OFF current of the switches in the TLC is identical to the injected reactive current in the dynamic process as pointed out by the green dots in Fig. 13(b). This indicates that the complementary switches are turned ON in the ZVS condition as discussed in Section II.

The steady-state experimental results are shown in Fig. 14 to verify ZVS in the TLCs, when the power reaches –1 p.u. In Fig. 14(a), the transformer current is successfully regulated in a sinusoidal form, and the ac-side voltage reference of the MMC is a superposition of a six-step voltage and a sinusoidal voltage coinciding with the analysis in Section II. The blocking voltage and the gate voltage of a switch in a TLC are shown in Fig. 14(b). The blocking voltage decreases to zero when the gate voltage is 0 V and the phase current is identical to the reactive current of 0.5 A, which means that the complementary switch is turned OFF at the reactive current. In addition, the investigated switch is turned ON when the blocking voltage fully reaches zero, which indicates a successful ZVS turn-ON.

Experimental results of the arm capacitor voltage balancing are presented in Fig. 15(a) and (b), when the balancing control is based on the injections of the fundamental-frequency and the fifth-order harmonic circulating currents, respectively. The controller parameters of the balancing controller, namely the PI controllers in Fig. 9 are set identical in order to observe the injected circulating current in the case of identical balancing dynamics. The balancing controller is activated at $t = 0.2$ s. As shown in Fig. 15, the upper and lower arm capacitor voltages converge to the balanced state with a similar time constant in both cases. However, the results in Fig. 15(b) actually include two different dynamic processes, where the boundary is indicated by the dashed blue lines. This is attributed to the fact that, the arm inductors employed in the downscale prototype are of high per-unit value impedances. Thus, the large reference of the fifth-order circulating current results in overmodulation at the initial stage of the balancing process.

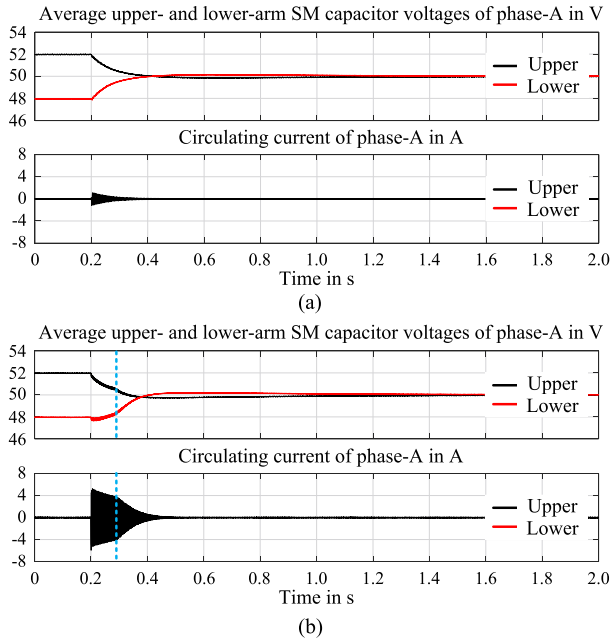

Fig. 15. Experimental results of the arm capacitor voltage balancing control, when the (a) fundamental-frequency and the (b) 5th-order circulating currents are injected for the voltage balancing.

It leads to a poor performance of the circulating current control and consequently a distorted balancing process of the arm capacitor voltages, whereas the voltage-balancing control employing the fundamental-frequency circulating current does not have this issue as shown in Fig. 15(a). Nevertheless, the magnitude of the fifth-order circulating current is still around five times of that of the fundamental-frequency current, which coincides with the analysis in Section IV. Thus, the validity of the proposed voltage-balancing control is verified, and the superiority of the injection of the fundamental-frequency circulating current over the fifth-order harmonic circulating current is proven.

VII. Conclusion

This paper presents a comprehensive discussion on the control of the TLC-MMC converter, which operates with six-step phase voltages and sinusoidal phase currents in the intermediate ac link. A closed-loop transformer-current control is presented, which is crucial for the low-power semiconductor losses of the TLC-MMC converter. It is first revealed in this paper that a six-step phase voltage on the ac side of the MMC can result in serious sixth-order voltage and current oscillations in the dc link, when the commonly used the direct-modulation-based operation is performed. The indirect-modulation-based operation is employed to solve this issue. However, it introduces the problem of arm capacitor voltage balancing. The principle and possible means for arm capacitor voltage balancing for the MMC operating with a six-step voltage are discussed, and the optimal control method and its implementation are proposed. The validity of the proposed control method is verified by simulations and experimental results tested by a downscale prototype.

References

[1] C. Meyer, "Key components for future offshore DC grids," *Ph.D. dissertation*, Inst. Power Electron. Elect. Drives, RWTH Aachen Univ., Aachen, Germany, 2007.
[2] H. Rao, "Architecture of Nan'ao multi-terminal VSC-HVDC system and its multi-functional control," *CSEE J. Power Energy Syst.*, vol. 1, pp. 9–18, 2015.
[3] R. W. De Doncker, "Power electronic technologies for flexible dc distribution grids," in *Proc. IEEE Int. Power Electron. Conf.*, 2014, pp. 736–743.
[4] S. Kenzelmann, "Modular dc/dc converter for dc distribution and collection networks," *Ph.D. dissertation*, Swiss Federal Inst. Technol., Lausanne, Switzerland, 2012.
[5] C. D. Barker, C. C. Davidson, D. R. Trainer, and R. S. Whitehouse, "Requirements of dc-dc converters to facilitate large dc grids," *CIGRE*, Paris, France, 2012.
[6] J. Ferreira, "The multilevel modular DC converter," *IEEE Trans. Power Electron.*, vol. 28, no. 10, pp. 4460–4465, Oct. 2013.
[7] J. Yang, Z. He, H. Pang, and G. Tang, "The hybrid-cascaded DC-DC converters suitable for HVdc applications," *IEEE Trans. Power Electron.*, vol. 30, no. 10, pp. 5358–5363, Oct. 2015.
[8] K. Filsoof and P. Lehn, "A bidirectional modular multilevel DC-DC converter of triangular structure," *IEEE Trans. Power Electron.*, vol. 30, no. 1, pp. 54–65, Jan. 2015.
[9] S. Norrga, L. Ängquist, and A. Antonopoulos, "The polyphase cascaded-cell dc-dc converter" in *Proc. IEEE Energy Convers. Congr. Expo.*, 2013, pp. 4082–4088.
[10] T. Lüth, M. M. C. Merlin, T. C. Green, F. Hassan, and C. D. Barker, "High-frequency operation of a DC/AC/DC system for HVDC applications," *IEEE Trans. Power Electron.*, vol. 29, no. 8, pp. 4107–4115, Aug. 2014.
[11] F. Sasongko, M. Hagiwara, and H. Akagi, "A front-to-front (FTF) system consisting of multiple modular multilevel cascade converters for offshore wind farms," in *Proc. IEEE Int. Power Electron. Conf.*, 2014, pp. 1761–1768.
[12] I. A. Gowaid, G. P. Adam, A. M. Massoud, S. Ahmed, and D. Holliday, "Quasi two-level operation of modular multilevel converter for use in a high-power DC transformer with DC fault isolation capability," *IEEE Trans. Power Electron.*, vol. 30, no. 1, pp. 108–123, Jan. 2015.
[13] S. P. Engel, M. Steineker, N. Soltau, S. Rabiee, H. Stagge, and R. W. De Doncker, "Comparison of the modular multilevel DC converter and the dual-active bridge converter for power conversion in HVDC and MVDC grids," *IEEE Trans. Power Electron.*, vol. 30, no. 1, pp. 124–137, Jan. 2015.
[14] S. Cui, N. Soltau, and R. W. De Doncker, "A high step-up ratio soft-switching dc-dc converter for interconnection of MVDC and HVDC grids," *IEEE Trans. Power Electron.*, vol. 33, no. 4, pp. 2986–3001, Apr. 2018.
[15] S. Debnath, J. Qin, B. Bahrani, M. Saeedifard, and P. Barbosa, "Operation, control, and applications of the modular multilevel converter: A review," *IEEE Trans. Power Electron.*, vol. 30, no. 1, pp. 37–53, Jan. 2015.
[16] A. Antonopoulos, L. Anguist, and H.P. Nee, "On dynamics and voltage control of the modular multilevel converter," in *Proc. EPE Eur. Conf. Power Electron. Appl.*, 2009, pp. 1–10.
[17] Q. Tu, Z. Xu, and Lie Xu, "Reduced switching-frequency modulation and circulating current suppression for modular multilevel converters," *IEEE Trans. Power Del.*, vol. 26, no. 3, pp. 2009–2017, Jul. 2011.
[18] M. Guan and Z. Xu, "Modeling and control of a modular multilevel converter-based HVDC system under unbalanced grid conditions," *IEEE Trans. Power Electron.*, vol. 27, no. 12, pp. 4858–4867, Dec. 2012.
[19] F. B. Ajaei and R. Iravani, "Enhanced equivalent model of the modular multilevel converter," *IEEE Trans. Power Del.*, vol. 30, no. 2, pp. 666–673, Apr. 2015.
[20] K. Ou *et al.*, "MMC-HVDC simulation and testing based on real-time digital simulator and physical control system," *IEEE J. Emerg. Sel. Top. Power Electron.*, vol. 2, no. 4, pp. 1109–1116, Dec. 2014.
[21] J. Xu, A. M. Gole, and C. Zhao, "The use of averaged-value model of modular multilevel converter in DC grid," *IEEE Trans. Power Del.*, vol. 30, no. 2, pp. 519–528, Apr. 2015.
[22] S. Li, X. Wang, Z. Yao, T. Li, and Z. Peng, "Circulating current suppressing strategy for MMC-HVDC based on nonideal proportional resonant controllers under unbalanced grid conditions," *IEEE Trans. Power Electron.*, vol. 30, no. 1, pp. 387–397, Jan. 2015.
[23] M. Saeedifard and R. Iravani, "Dynamic performance of a modular multilevel back-to-back HVDC system," *IEEE Trans. Power Del.*, vol. 25, no. 4, pp. 2903–2912, Oct. 2010.

[24] H. Kuhn, "Physikalische Modellbildung von IGCTs für die Schaltungssimulation," (in German), *Ph.D. dissertation*, Technische Universität München, Munich, Germany, 2002.
[25] J. Voss, J. Henn, and R. W. De Doncker, "Control techniques of the auxiliary-resonant commutated pole in the dual-active bridge," in *Proc. IEEE Int. Conf. Power Electron. Drive Syst.*, 2017, pp. 972–978.
[26] J. Voss, B. Bagaber, and R. W. De Doncker, "Full soft-switching capability of the dual-active bridge by using the auxiliary-resonant commutated-pole technique," in *Proc. Int. Symp. Power Electron. Distrib. Gener.*, 2017, pp. 1–8.
[27] J. Forrest and B. Allard, "Thermal problems caused by harmonic frequency leakage fluxes in three-phase, three-winding converter transformers," *IEEE Trans. Power Del.*, vol. 19, no. 1, pp. 208–213, Jan. 2004.
[28] Q. Song, W. Liu, X. Li, H. Rao, S. Xu, and L. Li, "A steady-state analysis method for a modular multilevel converter," *IEEE Trans. Power Electron.*, vol. 28, no. 8, pp. 3702–3713, Aug. 2013.
[29] T. B. Wood, D. E. Macpherson, D. Banham-Hall, and S. J. Finney, "Ripple current propagation in bipole HVDC cables and applications to DC grids," *IEEE Trans. Power Del.*, vol. 29, no. 2, pp. 926–933, Apr. 2014.
[30] Q. Tu, Z. Xu, Y. Chang, and L. Guan, "Suppressing DC voltage ripples of MMC-HVDC under unbalanced grid conditions," *IEEE Trans. Power Del.*, vol. 27, no. 3, pp. 1332–1338, Jul. 2012.
[31] S. Cui, S. Kim, J. J. Jung, and S. K. Sul, "A comprehensive cell capacitor energy control strategy of a modular multilevel converter (MMC) without a stiff dc bus voltage source," in *Proc. IEEE Appl. Power Electron. Conf. Expo.*, 2014, pp. 602–609.
[32] S. Cui and S. K. Sul, "A comprehensive DC short-circuit fault ride through strategy of hybrid modular multilevel converters (MMCs) for overhead line transmission," *IEEE Trans. Power Electron.*, vol. 31, no. 11, pp. 7780–7796, Nov. 2016.
[33] S. Cui, N. Soltau, and R. W. De Doncker, "Dynamic performance and fault-tolerant capability of a TLC-MMC hybrid DC-DC converter for interconnection of MVDC and HVDC gridsm" *Energy Convers. Congr. Expo.*, 2017, pp. 1622–1628.
[34] R. Lenke, "A contribution to the design of isolated dc-dc converters for utility applications," Ph.D. dissertation, E.ON Energy Research Center, RWTH Aachen Univ., Aachen, Germany, 2012.
[35] J. Jacobs, "Multi-phase series-resonant dc-to-dc converters," Ph.D. dissertation, Inst. Power Electron. Elect. Drives, RWTH Aachen Univ., Aachen, Germany, 2005.

Shenghui Cui (S'13) received the B.S. degree in electrical engineering from Tsinghua University, Beijing, China, in 2012, and the M.S. degree in electrical engineering from Seoul National University, Seoul, South Korea, in 2014, and the Dr.-Ing. degree in electrical engineering with the highest distinction (*summa cum laude*) from RWTH Aachen University, Aachen, Germany, in 2019.

Since March 2015, he has been with the Institute for Power Generation and Storage System, E.ON Energy Research Center, RWTH Aachen University, Aachen, Germany, as a Research Associate. His research interests include wide-bandgap power-semiconductor devices, and high-power converters for medium- and high-voltage applications.

Mr. Cui was the recipient of the Second Place Prize Paper Award of the IEEE TRANSACTIONS ON POWER ELECTRONICS, in 2018, the Second Prize Paper Award of IEEE IPEC (ECCE Asia), in 2018, and the Outstanding Presentation Award of IEEE APEC, in 2014.

Jingxin Hu (S'16) received the B.S. degree from Northeastern University, Shenyang, China, and the M.Sc. degree from RWTH Aachen University, Aachen, Germany, in 2010 and 2013, respectively, both in electrical engineering.

From April 2012 to October 2012, he was an Intern with the Corporate Research Center, ABB Switzerland Ltd., Baden-Dattwil, Switzerland. In 2013, he joined the General Electric Global Research Center, Munich, Germany, to work on his master's thesis. Since October 2014, he has been with the Institute for Power Generation and Storage Systems, E.ON Energy Research Center, RWTH Aachen University, as a Research Associate. His research interests include dc solid-state transformers, renewable power generation, and dc microgrids.

Rik W. De Doncker (F'01) received the Ph.D. degree in electrical engineering from the Katholieke Universiteit Leuven, Leuven, Belgium, in 1986.

In 1987, he was the Visiting Associate Professor with the University of Wisconsin—Madison, Madison, WI, USA. After a short stay as an Adjunct Researcher with the Interuniversity Microelectronics Centre, Leuven, Belgium, he joined, in 1989, the Corporate Research and Development Center, General Electric Company, Schenectady, NY, USA. In 1994, he joined the Silicon Power Corporation, a former division of General Electric Inc., as the Vice President of Technology. In 1996, he was a Professor at RWTH Aachen University, Aachen, Germany, where he currently leads the Institute for Power Electronics and Electrical Drives. Since 2006, he has been the Director of the E.ON Energy Research Center, RWTH Aachen University.

Dr. De Doncker was the President of the IEEE Power Electronics Society (PELS), in 2005 and 2006. He was the Founding Chairman of the German IEEE Industry Applications Society PELS Joint Chapter. In 2002, he was the recipient of the IEEE IAS Outstanding Achievement Award. In 2008, he was the recipient of the IEEE PES Nari Hingorani Custom Power Award. In 2009, he led a VDE/ETG Task Force on Electric Vehicles. In 2010, he received an Honorary Doctor degree of TU Riga, Latvia. In 2013, he was the recipient of the IEEE William E. Newell Power Electronics Award.